

A Natural 2D Heterostructure [Pb_{3.1}Sb_{0.9}S₄][Au_xTe_{2-x}] with Large Transverse Non-saturating Negative Magnetoresistance and High Electron Mobility

Haijie Chen,^{1,3} Jiangang He,² Christos D. Malliakas,¹ Constantinos C. Stoumpos,¹
Alexander J. E. Rettie,³ Jin-Ke Bao,³ Duck Young Chung,³ Wai-Kwong Kwok,³
Christopher Wolverton,² and Mercouri G. Kanatzidis^{*,1,2,3}

¹*Department of Chemistry, Northwestern University, Evanston, Illinois 60208, United States*

²*Department of Materials Science and Engineering, Northwestern University, Evanston, Illinois 60208, United States*

³*Materials Science Division, Argonne National Laboratory, Lemont, Illinois 60439, United States*

*Corresponding Author

Email: m-kanatzidis@northwestern.edu

Abstract: We report the two-dimensional (2D) natural heterostructure $[\text{Pb}_{3.1}\text{Sb}_{0.9}\text{S}_4][\text{Au}_x\text{Te}_{2-x}]$ ($x = 0.52 - 0.36$) which shows anomalous, transverse non-saturating negative magnetoresistance (MR). For $x = 0.52$, the material has a commensurately modulated structure with alternating $[\text{Pb}_{3.1}\text{Sb}_{0.9}\text{S}_4]$ rocksalt layers and atomically thin $[\text{Au}_x\text{Te}_{2-x}]$ sheets, as determined by single crystal X-ray diffraction using a $(3 + 1)$ -dimensional space group; for other x compositions, the modulated structures are absent and the Au and Te atoms are disordered. The transport properties in this system in low temperature (< 100 K) are dominated by an unusual 2D hopping mechanism, while at room temperature a high carrier mobility of $\sim 1352 \text{ cm}^2 \text{ V}^{-1} \text{ s}^{-1}$ is obtained ($x = 0.36$). The confined electrons within the $[\text{Au}_x\text{Te}_{2-x}]$ layers are also exposed to inter-layer coupling with the insulating $[\text{Pb}_{3.1}\text{Sb}_{0.9}\text{S}_4]$ layers and as a result the properties of the heterostructures emerge not only from the constituent layers, but also the interactions between them. Furthermore, the various Au and Te coordination patterns found in the $[\text{Au}_x\text{Te}_{2-x}]$ sheets as a function of x further contribute to a unique electronic structure that leads to the anomalous non-saturating negative MR with different field dependent behaviors. First-principles calculations indicate that the $[\text{Au}_x\text{Te}_{2-x}]$ sheets are responsible for the unusual electrical transport properties in this 2D system.

Keywords: 2D materials; high mobility; magnetoresistance

Introduction

Two-dimensional (2D) materials, such as the canonical graphene and transition metal dichalcogenides (TMD), some of which exist in nature as minerals, have novel quantum properties that can derive from their special electronic structures and Fermi surfaces.¹⁻⁶ Going beyond graphene and TMDs, new classes of 2D materials can harbor new physical and chemical phenomena, for example, the strong anharmonicity in SnSe results in intrinsically ultralow thermal conductivity and the record high figure of merit thermoelectricity.⁷⁻⁸ Also, the unique crystal structures of the layered SrMnBi₂ and SrMnSb₂ generate highly anisotropic Dirac cones, which lead to strong Shubnikov-deHaas oscillations.⁹⁻¹⁰ The discovery of intrinsic ferromagnetism in 2D Cr₂Ge₂Te₆,¹¹ and CrI₃¹²⁻¹⁴ opens up opportunities for potential spintronics applications.¹⁵⁻¹⁸ ZrSiS exhibits Si square nets and [ZrS] slabs and features Dirac nodes, without interference from other electronic bands, making it promising for investigating aspects of topological Dirac and Weyl physics.¹⁹⁻²¹

Naturally formed heterostructures made of heavy atoms are an exceptional class of 2D materials because they can provide special conditions for exploring novel quantum phenomena at the atomic scale. Of particular interest are those in which spin-orbit coupling is strong and have direct relevance to topological quantum phenomena. Previously, we reported that [Pb₂BiS₃][AuTe₂], known as the naturally occurring mineral buckhornite, hosts 2D carriers in single-atom-thick layers.²² The structure is composed of stacked weakly coupled [Pb₂BiS₃] layers and [AuTe₂] sheets. Magneto-transport measurements showed that [Pb₂BiS₃][AuTe₂] is a multiband semimetal with strong spin-orbit coupling.²³⁻
²⁴ Actually, in nature, there are several other interesting 2D materials, such as the so-called

cylindrite ($\text{FeSn}_4\text{Pb}_3\text{Sb}_2\text{S}_{14}$),²⁵ abramovite ($\text{Pb}_2\text{SnInBiS}_7$),²⁶ merelaniite ($\text{Mo}_4\text{Pb}_4\text{VSbS}_{15}$),²⁷ levyclaudite ($\text{Pb}_8\text{Sn}_7\text{Cu}_3(\text{Bi,Sb})_3\text{S}_{28}$),²⁸ jaszczakite ($[(\text{Pb,Bi})_3\text{S}_3][\text{AuS}_2]$),²⁹ to name a few. Recently, the mineral franckeite was demonstrated that it can be exfoliated into few layers towards efficient photodetectors.³⁰ These 2D minerals, however, are poorly understood, as neither the detailed structures nor the fundamental properties have been elucidated. Some exhibit complex superlattices arising from the strain caused by the mismatch between adjacent hetero-layers³¹⁻³² and refinement of modulated structures is usually a daunting challenge.³³⁻³⁴

Here we focus on synthetic nagyagite whose precise structure and actual formula remain undefined.³⁵⁻³⁶ We successfully grew single crystals and found a modulated structure which was solved using (3+1)-dimensional crystallography. The stoichiometry is found to be $[\text{Pb}_{3.1}\text{Sb}_{0.9}\text{S}_4][\text{Au}_x\text{Te}_{2-x}]$ ($x = 0.52 - 0.36$) in which the Au:Te ratio varies from 1:2.8 to 1:4.5 with a concurrent structural change from commensurately modulated superlattice to disordered states. For $x = 0.52$, the structure is commensurately modulated, forming quasi- $[\text{AuTe}_2]$ 1D stripes in the atomically thin $[\text{Au}_x\text{Te}_{2-x}]$ sheet. Charge transport measurements show that the mineral nagyágite is an n-type semiconductor with a high room temperature electron mobility of $\sim 1352 \text{ cm}^2 \text{ V}^{-1} \text{ s}^{-1}$ (for $x = 0.36$). In this narrow gapped semiconducting, nonmagnetic system, we observed for the first time a large non-saturating negative MR with the magnetic field applied perpendicular to the current flow (transverse).²³⁻²⁴

Experimental Section

Synthesis. The self-flux method was used to synthesize single crystals of $[\text{Pb}_2(\text{Pb,Sb})\text{S}_4][(\text{Au,Te})_2]$.²³ Five different compositions of nominal $\text{Pb}_3\text{SbS}_4\text{Au}_x\text{Te}_{2-x}$ ($x = 0.57, 0.5, 0.44, 0.4, \text{ and } 0.333$) were synthesized in stoichiometric reactions of Pb, Sb, S, Au, and Te with Au:Te ratios of 1:2.5, 1:3, 1:3.5, 1:4, and 1:4.5, respectively. For instance, to synthesize the nominal compound $\text{Pb}_3\text{SbS}_4\text{Au}_{0.4}\text{Te}_{1.6}$, 3 mmol Pb (0.6216 g), 1 mmol Sb (0.1218 g), 4 mmol S (0.1283 g), 0.4 mmol Au (0.079 g), and 1.6 mmol Te powders (0.204 g) were placed into a fused silica tube. The tube was evacuated to $\sim 10^{-4}$ Torr and then flame sealed. The sealed tube was put into a programmable furnace and heated to 850 °C for 10 h, held at this temperature for 2 h, slow cooled to 600 °C for 80 h and then cooled to room temperature by naturally turning off the furnace. Plate-shaped black single crystals of $[\text{Pb}_2(\text{Pb,Sb})\text{S}_4][(\text{Au,Te})_2]$ with mirror-like surfaces formed only at the top surface of the final ingots. The main byproducts were $\text{Pb}_{1-x}\text{Sb}_x\text{S}$, PbS, and AuTe_2 . Attempts to synthesize samples with other Au:Te ratios than the x values mentioned above were unsuccessful.

Scanning Electron Microscopy-Energy Dispersive X-ray Spectroscopy (SEM-EDS).

Crystal imaging and elemental analysis of the synthesized crystals were performed by scanning electron microscope (SEM) and energy dispersive spectroscopy (EDS) using a Hitachi S3400N-II scanning electron microscope equipped with an Oxford Instruments INCAx-act SDD EDS detector. The samples were mounted with a carbon tape on an aluminum stub. Elemental analysis was performed on several crystals at an accelerating voltage of 20 kV, a probe current of 80 mA and an acquisition time of 120 seconds.

Single-Crystal X-ray Diffraction. Because of the soft feature and layered structure for this mineral, the single crystals were cut from the ingots with a razor blade under extreme caution. Afterwards, a single crystal ($600 \mu\text{m} \times 500 \mu\text{m} \times 100 \mu\text{m}$) was mounted on a glass

fiber. Diffraction data was collected on the single-crystal diffractometer (STOE IPDS 2T) at room temperature (293 K) with graphite-monochromatized Mo K_α radiation ($\lambda = 0.71073$ Å) at 50 kV and 40 mA.³⁷ Each data frame was collected with an exposure time of 5 min and ω rotation of 1°. The X-RED and X-SHAPE software packages were used for data integration and analytical absorption corrections.³⁷ The data was reduced, integrated, and corrected for absorption using the STOE X-Area suite.³⁷ The crystal structures were solved and refined by full-matrix least-squares on F^2 using the Jana2006 package³⁸⁻³⁹. Summarized crystal structure and refinement data are given in Tables S1-S6.

Electrical Transport Measurements. Charge transport property measurements, including the resistivity, Hall effect, and magnetoresistance, were carried out on the single crystals. The data was obtained using a Dynacool Physical Property Measurement System (PPMS, Quantum Design) from 2 to 300 K. The resistivity was measured in a four-point collinear geometry. The Hall effect from ± 9 T was measured by placing two voltage contacts perpendicular to the plate crystal and the plane of current flow. The Hall resistivity, ρ_{xy} , was obtained via $\rho_{xy} = [\rho_{(+H)} - \rho_{(-H)}]/2$. The magnetoresistance, defined by $\Delta\rho/\rho_0 = [\rho(H) - \rho(0)]/\rho(0) \times 100\%$,⁴⁰⁻⁴¹ was measured with the current along the a axis and the field along the c axis. The direct use of silver paste on $[\text{Pb}_2(\text{Pb,Sb})\text{S}_4][(\text{Au,Te})_2]$ resulted in poor contact because of the smooth surface of the single crystals. To form stable Ohmic contact, Pt pads (~ 50 nm thick) were sputtered before 25 μm gold wires were attached using Ag paste (DuPont 4929N).⁴²⁻⁴³ Relevant dimensions (length, width, and thickness) were measured from an SEM image of the sample.

Computational methods: All density functional theory (DFT) calculations are performed using the Vienna *Ab-initio* Simulation Package (VASP),⁴⁴⁻⁴⁵ with a plane wave basis set

and projector-augmented wave (PAW) pseudo potentials.⁴⁶⁻⁴⁷ The Perdew-Burke-Ernzerhof (PBE) exchange-correlation functional is used for crystal structure relaxation and electronic structure calculations.⁴⁸ In order to approximate the crystal structure of $\text{Pb}_3\text{SbS}_4\text{Au}_x\text{Te}_{2-x}$ ($x = 0.5$ and 0.4) with partially occupied Te, Au, Pb, and S atoms, a $2 \times 2 \times 1$ supercell ($\text{Pb}_{12}\text{Sb}_4\text{S}_{16}\text{Au}_2\text{Te}_6$) and a $2 \times 5 \times 1$ supercell ($\text{Pb}_{30}\text{Sb}_{10}\text{S}_{40}\text{Au}_4\text{Te}_{16}$) were employed for Au:Te = 1:3 and Au:Te = 1:4. The Γ -centered k -meshes of $8 \times 8 \times 4$ and $8 \times 3 \times 4$ were used for the supercells with Au:Te = 1:3 and Au:Te = 1:4, respectively. All crystal structures were fully relaxed until the force on each atom was less than 0.01 eV/\AA .

Results and Discussion

Crystal Structure and Exfoliation. $[\text{Pb}_{3.1}\text{Sb}_{0.9}\text{S}_4][\text{Au}_x\text{Te}_{2-x}]$ has a unique structure. As displayed in the SEM image of Figure 1a, the single crystals show smooth surfaces with typical size of approximately $1 \text{ mm} \times 0.5 \text{ mm} \times 0.05 \text{ mm}$. As shown in the same image, the thick area of the crystal displays golden or black color. Energy dispersive X-ray spectroscopy (EDS) mapping confirmed the existence of the Pb, Sb, S, Au and Te elements and their uniform distribution in the crystals. The EDS results on all single crystals examined (Figure S1) gave a consistent ration of Pb, Sb, and S with $\sim 3:1:4$, while the Au and Te ratio varies from $\sim 1:3$ to $1:4.5$, which was also observed in previous report.³⁶ Because of the layered morphology, it is possible to mechanically exfoliate using the well-known Scotch-tape method (Figure S2).^{3, 49} This process successfully produced ultrathin crystals with sea-green contrast under visible light (see the inset of Figure 1a).

Using single crystal X-ray diffraction, we were able to solve and refine the crystal structures of the various $[\text{Pb}_{3.1}\text{Sb}_{0.9}\text{S}_4][\text{Au}_x\text{Te}_{2-x}]$ ($x = 0.52 - 0.36$) compositions. For the

single crystal obtained with the starting Au:Te ratio of 1:2.5, the formula was refined to be $[\text{Pb}_{3.1}\text{Sb}_{0.9}\text{S}_4][\text{Au}_{0.52}\text{Te}_{1.48}]$ in which the Au:Te ratio was determined to be 1:2.8. The crystal structure is composed of alternating stacks of “[$\text{Pb}_{3.1}\text{Sb}_{0.9}\text{S}_4$] layers” and “[$\text{Au}_{0.52}\text{Te}_{1.48}$] sheet” along the c -axis, as delineated in Figure 1b. The [$\text{Pb}_{3.1}\text{Sb}_{0.9}\text{S}_4$] layers are formed by pairs of distorted rocksalt-type PbS layers, whilst Au and Te atoms are disordered on a single-atom thickness square net that develops in between the pairs of rocksalt sheets. The bond distances and atom labeling are shown in Figure 1c, where, in the rocksalt layer, Sb selectively mixes with the Pb2 site (facing towards the second rocksalt sheet) whereas Pb1 atoms (facing towards the square net) are fully occupied. The square nets, which are atomically thin, consist of a single atomic site (Figure 1d) shared between Au and Te. In the case of [$\text{Au}_{0.52}\text{Te}_{1.48}$] sheet, the bonds show alternating distances along a axis, with 2.940(8) and 2.944(7) Å, respectively. The shortest bond distance between the [$\text{Pb}_{3.1}\text{Sb}_{0.9}\text{S}_4$] layers and [$\text{Au}_{0.52}\text{Te}_{1.48}$] sheets is 3.614(3) Å which is slightly larger than the corresponding distance between the [$\text{Pb}_{3-x}\text{Sb}_{1+x}\text{S}_4$] layer and Te sheet in the charge density wave system $\text{Pb}_{3-x}\text{Sb}_{1+x}\text{S}_4\text{Te}_{2-\delta}$ (3.597(2) Å).³⁴ This indicates relatively weak interlayer interactions and allows for the material to be easily cleaved. Figure 1e shows a composed precession-like image of the reciprocal lattice (from the raw X-ray diffraction data) along the b axis ([0 1 0]) at room temperature ($x = 0.52$). The diffraction pattern in the image shows that there are obvious extra satellite diffraction peaks around the main Bragg diffraction peaks, indicating the existence of a modulated structure. As listed in Table 1, a (3 + 1)-dimensional symmetry was applied for the data integration with one commensurate q -vector of $1/3a^* - 1/3c^*$, which indicates an actual $3 \times 1 \times 3$ superlattice.

Because of the good diffraction properties of the specimen, we succeeded in including these extra satellite peaks in our structure solution and refined the detailed modulated structure, using the (3 + 1)-dimensional superspace crystallographic technique. In this case, the position of the atoms is described with a combination of static waves using the atoms in the undistorted unit cell (subcell) as a reference. A total of 14870 independent reflections were collected with 4930 main and 9940 satellites. The final agreement factor converged to a good value of 5.20% for all observed reflection ($I > 2\sigma(I)$), suggesting good refinement based on the high-quality X-ray diffraction data ($R_{\text{int}} = 0.0818$). The modulated structure adopts the (3 + 1)-dimensional superspace group $P2_1/m(\alpha 0\gamma)00$.

Though all atoms are displaced from their average (undistorted) position, the refinement results demonstrate that the modulation mainly arises from the Au/Te sheets. The wave dependent Au/Te occupancy and bond distances are given in Figure 2a and 2b, respectively. The occupancy of Au/Te changes between 0.5/0.5 and 0.98/0.02. The Au/Te–Au/Te bond distance is distributed in the range of 2.725(6) and 3.179(2) Å. The modulation on the distances between Au/Te atoms with the displacements along the *a*, *b*, and *c* axes is illustrated in Figure 2c. The separation of the atoms is significantly large along the *a* axis, with variance of ± 0.2 Å, which demonstrates that the distortion of Au/Te atoms is only limited to the *a* direction.

A fragment of the commensurately modulated structure is shown in Figure 2d. The subcell of the modulated structure is a $3 \times 1 \times 3$ matrix based on the average (undistorted) cell. The $[\text{Pb}_{3.1}\text{Sb}_{0.9}\text{S}_4]$ layers and $[\text{Au}_{0.52}\text{Te}_{1.48}]$ sheets are shown in Figure 2e and 2f, respectively. The structure exhibits a unique pattern of short and long Au/Te–Au/Te distances and occupancies fluctuations. Au/Te atoms driven by the modulation feature a

parallel [AuTe₂]-like chain along the *b* axis. As shown in Figure 2f, the center atom (green) is surrounded by four atoms (indigo) in the chains. The bond distances within the chains are around 2.83 Å, while those between the chains around 3.17 Å. The center site in the [AuTe₂]-like chain tends to be occupied by more Au atoms with Au/Te ratio of 0.5/0.5; while fewer Au atoms are found in the sites at the edge with Au/Te ratio of around 0.15/0.85. Au atoms therefore prefer to occupy the center positions and Te atoms go to the edges. Compared to the [Au_{0.52}Te_{1.48}] sheets, the distortion within the [Pb_{3.1}Sb_{0.9}S₄] layers are much weaker. The tendency to form the [AuTe₂]-like chains is the driving force forming the modulated structure rather than the interaction between adjacent [Pb_{3.1}Sb_{0.9}S₄] layers and [Au_{0.52}Te_{1.48}] sheets.

For the other compositions of [Pb_{3.1}Sb_{0.9}S₄][Au_{*x*}Te_{2-*x*}] with less Au content, the satellite reflections were absent in the X-ray diffraction images, indicating lack of modulation in the structures. In these cases, the Au and Te atoms were assigned to the same site and can be viewed as disordered. We refined the Au/Te of 1:4 composition with the space group of *P2₁/m* as the representative one, giving [Pb_{3.1}Sb_{0.9}S₄][Au_{0.44}Te_{1.56}] with the same Pb/Sb ratio, which is consistent with the EDS results, see Table 1. The Pb and Sb ratio is also refined to be 3.1:0.9. The distances of the Pb1-S1 bonds are refined to be 2.995(9), 2.993(9) and 2.899(5) Å, respectively (Figure S3 and S4). Considering the EDS results, the correct formula for nagyágite is [Pb_{3.1}Sb_{0.9}S₄][Au_{*x*}Te_{2-*x*}] (*x* = 0.52 – 0.36).

The electronic state of [AuTe₂]⁻ chains within the Te square sheets in [Pb_{3.1}Sb_{0.9}S₄][Au_{*x*}Te_{2-*x*}] was probed with XPS measurements which elucidate the valence states of the atoms present in the square net. Figure S5 shows the XPS of the [Pb_{3.1}Sb_{0.9}S₄][Au_{0.52}Te_{1.48}] and [Pb_{3.1}Sb_{0.9}S₄][Au_{0.44}Te_{1.56}] single crystals. The full scan

confirms the existence of the Pb, Sb, S, Au, Te atoms (Figure S5a). In the case of Pb, two peaks with binding energies of 137.8 eV and 142.7 eV corresponding to $\text{Pb}^{2+} 4f_{7/2}$ and $4f_{5/2}$, respectively, were observed (Figure S5b). The S 2p peak can be deconvoluted into two peaks at 162.3 eV and 161.1 eV (Figure S5c), corresponding to the $\text{S}^{2-} 2p_{1/2}$ and $2p_{3/2}$ orbitals, respectively. The binding energies of 539.1 and 530.1 eV for Sb are attributed to $\text{Sb}^{3+} 3d_{5/2}$ and $3d_{3/2}$ core states (Figure S5d). The energy range for Au is shown in Figure S5e, where the observed binding energies 84.7 and 88.4 eV correspond to a single Au^{3+} oxidation state $4f_{7/2}$ and $4f_{5/2}$ core states. The absence of any other valence signal for Au demonstrate the absence of Au-Au bonds (Au^{2+} or Au^+ oxidation state) in nagyágite. For Te, the peaks at 572.5 and 575.9 eV arise from Te^{2-} and $\text{Te}^- 3d_{5/2}$ core states, while those at 582.9 and 586.3 eV from Te^{2-} and $\text{Te}^- 3d_{3/2}$ core states, see Figure S5f. Te in these two oxidation states contribute to a negatively charged square net which is the only mixed valence species present in the compound. Thus, based on the XPS results, the chemical formula is thus $(\text{Pb}^{2+})_{3.1}(\text{Sb}^{3+})_{0.9}(\text{S}^{2-})_4(\text{Au}^{3+})_x(\text{Te}^-)_a(\text{Te}^{2-})_b$ ($a = 3.1 - 5x$, $b = 4x - 1.1$). The exact amounts of Au^{3+} , Te^- , and Te^{2-} are listed in Table 2. The XPS results directly confirm that Au and Te ratio can be varied and leads to unusual mixed cation/anion feature in the nagyágite system.

Charge Transport Properties. Figure 3a shows the temperature dependent resistivity (ρ) of all $[\text{Pb}_{3.1}\text{Sb}_{0.9}\text{S}_4][\text{Au}_x\text{Te}_{2-x}]$ samples from 300 to 2 K. The inset gives the corresponding temperature dependent conductivity (σ). ρ increases with decreasing temperature, indicating semiconducting behaviors. With decreasing Au content, the semiconducting behavior becomes more pronounced. As listed in Table 2, for $x = 0.52$, ρ increases from 0.00577 Ω cm at 300 K to 0.054 Ω cm at 2 K; for $x = 0.36$, ρ increases

dramatically from 0.0126 Ω cm at 300 K to 8.26×10^4 Ω cm at 2 K. This result suggests the presence of a bandgap in these samples which becomes wider with decreasing Au content. Electronic absorption spectroscopy, however, did not show any obvious bandgap above 0.05 eV, mainly because of interference from free carriers.³⁴ On the basis on the classical semiconductor equation,⁵⁰

$$\rho = \rho_0 \exp\left(\frac{E_a}{k_B T}\right),$$

where ρ_0 , E_a , k_B and T denote the pre-exponential factor, activation energy, Boltzmann constant and temperature, respectively. Based on the data in the high temperature range (100 – 300 K), the value of E_a was determined to be between 0.007 and 0.019 eV for samples with Au:Te ratio from 1:2.8 to 1:4.5 (Figure S6).

As shown in Figure 3b, the data of σ between 2 and 100 K can be well fitted by a 2D variable range hopping mechanism.⁵¹ The thermally activated conductivity can be expressed by:

$$\sigma = \sigma_0 \exp\left(-\frac{T_0}{T}\right)^{1/\alpha},$$

where α is related to the dimensionality of transport (it equals 2, 3, and 4 for 1D, 2D, and 3D lattices), and σ_0 and T_0 are empirical constants related to the carrier density and localization length of the hopping electron.⁵¹⁻⁵² The fitting details are given in Figure S7. For the samples of $x = 0.44$ and 0.4, it can be divided into two regions with both crossovers occurring at ~ 8 K, which could be related to the variance of the hopping distance. It is noted that variable hopping distance is found in some promising disordered insulators.⁵³ Herein, the phenomenon of different hopping distance in this compound should be due to the Au and Te disorder. The good fit with this model confirms the layered nature of the

structure and weak coupling between the adjacent $[\text{Pb}_{3.1}\text{Sb}_{0.9}\text{S}_4]$ and $[\text{Au}_x\text{Te}_{2-x}]$ layers, similar as those found in the 2D $\text{CrCl}_2(\text{pyrazine})_2$ ⁵⁴ and $[\text{Tl}_4\text{Sb}_6\text{Se}_{10}][\text{Sn}_5\text{Sb}_2\text{Se}_{14}]$ ⁵².

The Hall effect was measured to determine the carrier concentration (n) and mobility (μ) as well as the x dependent variances for the same samples previously measured for resistivity. The in-plane Hall resistivity (ρ_{xy}) shows linear field dependence (Figure S8). The negative ρ_{xy} at positive field indicates that electrons are the dominant charge carriers. As shown in Figure 3c, n decreases with decreasing temperature from 300 to 2 K, which is due to the thermal excitation (see inset). For $x = 0.52$, n at 300 K is determined to be $4.14 \times 10^{18} \text{ cm}^{-3}$ and decreases to $8.14 \times 10^{17} \text{ cm}^{-3}$ at 2 K. With decreasing Au fraction, for example $x = 0.36$, n decreases dramatically from $3.67 \times 10^{17} \text{ cm}^{-3}$ at 300 K to $4.16 \times 10^{13} \text{ cm}^{-3}$ at 2 K.

The mobility μ (estimated by $\mu = 1/(nq\rho)$) decreases with decreasing temperature for all samples, Figure 3d. A maximum value of $1352 \text{ cm}^2 \text{ V}^{-1} \text{ s}^{-1}$ was obtained at 300 K for $x = 0.36$. When the Au amount increases to the maximum 0.52, μ decreases to $261.2 \text{ cm}^2 \text{ V}^{-1} \text{ s}^{-1}$ at 300 K. This result suggests that the μ is strongly related to the degree of disorder. Higher degree of disorder with large Au:Te ratios generates smaller μ .

The most striking result is the temperature dependence of the mobility, which continues to rise on heating despite already being very high. This is highly unusual behavior since mobility is expected to fall with increasing temperatures due to classical acoustic phonon scattering. In a typical semiconductor with mobilities $<100 \text{ cm}^2 \text{ V}^{-1} \text{ s}^{-1}$, decreasing μ with decreasing temperature is usually attributed to impurity scattering mechanisms.⁵⁵ Here, in this material, however, the temperature dependence of the mobility should be dominated by another mechanism. Furthermore, as shown in the inset in Figure

3c, n increases with increasing temperature between 100 and 300 K. Generally, the extra thermally activated carriers increase carrier-carrier scattering and decrease the mobility. The observed unusual mobility behavior suggests increasingly weak scattering at higher temperatures, compared to conventional semiconductors. To explore what happens upon heating, we carried out temperature-dependent X-ray diffraction on the modulated $\text{Pb}_{3.1}\text{Sb}_{0.9}\text{S}_4\text{Au}_{0.52}\text{Te}_{1.48}$. Figure S9 shows the synthetic precession images of the reciprocal lattice along the c -axis ($[0\ 0\ 1]$) from 100 to 500 K. As indicated by the arrows, there are extra satellite peaks around the main Bragg diffraction peaks because of the modulation, but these peaks weaken gradually with rising temperature. If we consider the dependence of the relative intensity ratio (R. I.) for the satellites to the main Bragg diffractions, Figure S10, we can see it decreases steadily with increasing temperature, indicating that the modulation gradually weakens and the monoatomic $[\text{Au}_x\text{Te}_{2-x}]$ sheet becomes smoother with more equal bond lengths between Au and Te. Thus, the continuous rise of mobility in this material is attributed to the diminishing degree of structural modulation in the square Au and Te.

Negative Magnetoresistance. Magneto-transport measurements on $[\text{Pb}_{3.1}\text{Sb}_{0.9}\text{S}_4][\text{Au}_x\text{Te}_{2-x}]$ crystals reveal anomalous behavior in the temperature dependence of magnetoresistance (MR). The $[\text{Pb}_{3.1}\text{Sb}_{0.9}\text{S}_4][\text{Au}_{0.52}\text{Te}_{1.48}]$ and $[\text{Pb}_{3.1}\text{Sb}_{0.9}\text{S}_4][\text{Au}_{0.5}\text{Te}_{1.5}]$ have been selected as representative for the discussion. The magnetic field dependence of MR at different temperatures are shown in Figure 4a and 4b, respectively. When the magnetic field (0 – 9 T) is applied perpendicular to the direction of the current flow, all MR exhibits negative values with no sign of saturation up to 9 T. For the structurally modulated $[\text{Pb}_{3.1}\text{Sb}_{0.9}\text{S}_4][\text{Au}_{0.52}\text{Te}_{1.48}]$ single crystal, the MR is highly sensitive to

temperature. As shown in Figure 4c, a maximum MR of $\sim -26\%$ was obtained at 9 T and 2 K. This diminishes sharply to -0.2% as the temperature rises to 50 K.

Interestingly, the transverse MR of $[\text{Pb}_{3.1}\text{Sb}_{0.9}\text{S}_4][\text{Au}_{0.52}\text{Te}_{1.48}]$ at 2 K shows two regions with different field dependence: in the low field ($0 \text{ T} < B < 2.2 \text{ T}$), the data show B^2 dependence; in the high field ($2.2 \text{ T} < B < 9 \text{ T}$), it shows $B^{0.5}$ dependence, Figure 4d. Similar MR behavior has been observed in the Weyl semimetal WTe_2 which shows highly anisotropic MR,^{6, 56-57} but in this case the measured MR is longitudinal with the field parallel to the current direction. In the case of $[\text{Pb}_{3.1}\text{Sb}_{0.9}\text{S}_4][\text{Au}_x\text{Te}_{2-x}]$ the MR is transverse. As far as we know, no similar MR behavior has been reported in transverse measurement mode with the field applied perpendicular to the direction of current. Furthermore, as shown in Figure 4e, in the low field region ($-0.5 \text{ T} < B < 0.5 \text{ T}$), the data show a small cusp-like feature as a result of positive MR. This cusp behavior possibly arises from weak anti-localization (WAL), as was proposed for ZrTe_5 .⁵⁸

As shown in Figure 4c, for the $[\text{Pb}_{3.1}\text{Sb}_{0.9}\text{S}_4][\text{Au}_{0.5}\text{Te}_{1.5}]$ sample with the disordered Au and Te atoms, the negative MR is less sensitive to temperature than that of $[\text{Pb}_{3.1}\text{Sb}_{0.9}\text{S}_4][\text{Au}_{0.52}\text{Te}_{1.48}]$. The MR of $[\text{Pb}_{3.1}\text{Sb}_{0.9}\text{S}_4][\text{Au}_{0.5}\text{Te}_{1.5}]$ at 2 K is proportional to $-B^{1.5}$, as shown in Figure 4f. The MRs for the other samples with disordered Au and Te atoms all show the same behavior with $-B^{1.5}$ dependent MR without any sign of saturation up to 9 T, Figure S11. For the classic model, the conventional negative MR is generally quadratic in B . Since the field dependence of the $[\text{Pb}_{3.1}\text{Sb}_{0.9}\text{S}_4][\text{Au}_x\text{Te}_{2-x}]$ samples deviates strongly from the classic model, it may indicate this material is a special 2D electron system, similar to GaAs/AlGaAs quantum wells.⁵⁹

Because magnetic field usually plays a role on localizing electrons and leads to positive MR, negative MR is considered an unusual phenomenon often related to peculiar physics.⁶⁰ Until now, negative MR has been reported in magnetic semiconductors⁶¹⁻⁶² and special semimetals and in most case is longitudinal in nature⁶³⁻⁶⁵. In this work, we observed for the first time a large non-saturating negative MR in a new narrow gapped semiconducting, nonmagnetic system with the magnetic field applied perpendicular to the current flow. Carrier mobility and disorder play crucial roles in negative MR.^{57, 60} In $[\text{Pb}_{3.1}\text{Sb}_{0.9}\text{S}_4][\text{Au}_x\text{Te}_{2-x}]$, the mobility changes significantly with x , but not MR. As shown in Figure S11d, MR at ± 9 T and 2 K increases slowly with decreasing Au:Te ratio from $\sim 26\%$ for $x = 0.52$ to $\sim -10\%$ for $x = 0.36$. Considering the decrease of electron mobility with Au:Te ratio, the role of carrier mobility in the MR behavior can be ruled out, and instead the MR should be influenced mainly by the disorder of Au and Te atoms in the atomically thin sheets of the structure where a higher degree of disorder leads to enhanced MR.

First-Principles Calculations. Because the experimental results indicate that the $[\text{Au}_x\text{Te}_{2-x}]$ layers determine the foundational properties in this heterostructure, in order to gain deeper insight into their role, we calculated the electronic structures of $[\text{Pb}_{3.1}\text{Sb}_{0.9}\text{S}_4][\text{Au}_x\text{Te}_{2-x}]$ using first-principles DFT methods. We used two different compositions: Au:Te = 1:4 (Figure S12) and Au:Te = 1:3 (Figure S13) while the Pb and Sb ratio was 3:1. Superlattices were used with 100% occupancy for all atoms to deal with the partial occupancy, see computational methods for details.

The band structures (without band unfolding back to the primitive cell) and partial density of states (PDOS) of Au:Te = 1:4 and Au:Te = 1:3 are depicted in Figure 5. The

electronic structures of these two compositions are similar and the role of spin-orbit coupling is very strong: both the valence and conduction bands near the Fermi level are mainly from Au $5d$ and Te $4p$ orbitals, whereas contributions from Pb, Sb, and S states are far away from the Fermi level. Therefore, the electrical conductivities of both compositions arise essentially from the $[\text{Au}_x\text{Te}_{2-x}]$ layers. The distorted rock-salt layers of $[\text{Pb}_3\text{SbS}_4]$, which are wide gap semiconductors, provide an insulating barrier and confines the electrons within the atom-thin 2D layers. This can be further clearly seen from the isosurface of the charge density of the bands around the Fermi level, see Figures 5a and c, and well explains the 2D hopping conductance in this system. It is clear that the electronic bands show nearly no dispersion along the Γ -Z direction (the layer stacking direction along c -axis in real space), implying a weak coupling between the $[\text{Au}_x\text{Te}_{2-x}]$ and $[\text{Pb}_3\text{SbS}_4]$ layers due to the large distance and therefore weak bonding between them.

The band gap opening in the Au:Te = 1:4 case, Figure 5b stems from distortions in the $[\text{Au}_{0.4}\text{Te}_{1.6}]$ layer after structure relaxation, which is analogous to the metal-to-insulator transition induced by a Peierls distortion.⁶⁶ In contrast, a metallic electronic structure is predicted in the unrelaxed structure where Au:Te = 1:4, see the density of states (DOS) in Figure S14. Moreover, the band gap decreasing with more Au is consistent with the experimental observation that the lower Au:Te ratio makes the system more semiconducting. With increasing temperature, we can expect this narrow bandgap (which derives from the modulated structure) to gradually close by the elimination of the modulation and equalization of the Au-Te bonds as discussed above, which gradually reduces the carrier scattering with rising temperature observed in the experimental data.

Conclusions

The naturally formed 2D heterostructure $[\text{Pb}_{3.1}\text{Sb}_{0.9}\text{S}_4][\text{Au}_x\text{Te}_{2-x}]$ ($x = 0.52 - 0.36$) found as the mineral nagyagite can be synthesized as single crystals in a series of compositions with different Au:Te ratios from 1:2.8 to 1:4.5. This phase width results in structure evolution from a modulated supercell to disordered ones. The samples are narrow band gap semiconductors and the semiconducting behavior becomes stronger with decreasing Au content. A room temperature carrier mobility of $\sim 1352 \text{ cm}^2 \text{ V}^{-1} \text{ s}^{-1}$ was obtained for the Au:Te ratio of 1:4.5 with a steadily increasing trend above room temperature. 2D hopping mechanism dominates the transport at low temperatures. All samples exhibit an unusual transverse non-saturating negative MR with field up to 9 T, which may be due to the unique mixing of Au and Te atoms in the same crystallographic sites in the atomically thin $[\text{Au}_x\text{Te}_{2-x}]$ sheets. The MR displays a diverse set of B^n ($n = 0.5, 1.5, 2$) dependent behaviors between the modulated version of the compound and the disordered, unmodulated ones. The strong 2D nature of this material is supported by the calculated DOS near the Fermi level for $[\text{Pb}_{3.1}\text{Sb}_{0.9}\text{S}_4][\text{Au}_x\text{Te}_{2-x}]$ which are dominated almost exclusively by the Au $5d$ and Te $4p$ orbitals regardless of x . Future work will focus on understanding the link of spin orbit coupling in this system and the transverse non-saturating negative MR including studies at magnetic fields >9 T. This work highlights the interesting opportunities in finding unusual effects and new physical properties in 2D heterostructures and the revelation of $[\text{Pb}_{3.1}\text{Sb}_{0.9}\text{S}_4][\text{Au}_x\text{Te}_{2-x}]$ as a new platform opens the field for deeper explorations of exotic physical transport behavior. For example, $[\text{Pb}_{3.1}\text{Sb}_{0.9}\text{S}_4][\text{Au}_x\text{Te}_{2-x}]$ may have quantum topological properties, however, to explore this

requires an extensive set of transport and spectroscopy experiments, which are out of the scope of this report.

ASSOCIATED CONTENT

Supporting Information. Refinement details of the modulated crystal structure, experimental section, EDS, a photo of the tape after exfoliation, side-view of the crystal structure for $[\text{Pb}_{3.1}\text{Sb}_{0.9}\text{S}_4][\text{Au}_{0.44}\text{Te}_{1.56}]$, Au/Te sheets vary with the Au:Te ratios, X-ray photoelectron spectra, evaluation of the values of the activation energy E_a , analysis of the conductivity based on the 2D electron variable range hopping mechanism, temperature dependence of the Hall resistivity, X-ray diffraction images of a $[\text{Pb}_{3.1}\text{Sb}_{0.9}\text{S}_4][\text{Au}_{0.52}\text{Te}_{1.48}]$ single crystal along the $[0\ 0\ 1]$ zone from 100 to 500 K, temperature dependence of the relative intensity (R. I.) for the intensity ratios of the satellites to the main diffractions in $[\text{Pb}_{3.1}\text{Sb}_{0.9}\text{S}_4][\text{Au}_{0.52}\text{Te}_{1.48}]$, field dependence of the magnetoresistance, crystal structure of the $2 \times 5 \times 1$ supercell for $\text{Pb}_{30}\text{Sb}_{10}\text{S}_{40}\text{Au}_4\text{Te}_{16}$, crystal structure of the $2 \times 2 \times 1$ supercell for $\text{Pb}_{12}\text{Sb}_4\text{S}_{16}\text{Au}_2\text{Te}_6$, the density of states (DOS) for $\text{Pb}_{30}\text{Sb}_{10}\text{S}_{40}\text{Au}_4\text{Te}_{16}$, crystallographic data and structure refinement, atomic coordinates, occupancy and equivalent isotropic displacement parameters, anisotropic displacement parameters, Fourier components of the displacive modulation (PDF)

Crystallographic data for $\text{Pb}_{3.1}\text{Sb}_{0.9}\text{S}_4\text{Au}_{0.52}\text{Te}_{1.48}$ and $\text{Pb}_{3.1}\text{Sb}_{0.9}\text{S}_4\text{Au}_{0.44}\text{Te}_{1.56}$ (CIF)

AUTHOR INFORMATION

Corresponding Author

*E-mail: m-kanatzidis@northwestern.edu

Author Contributions

The authors declare no competing financial interest.

Acknowledgements

Work at Argonne National Laboratory primarily was supported by the U.S. Department of Energy, Office of Science, Basic Energy Sciences, Materials Sciences and Engineering Division. SEM-EDS work was performed by use of the EPIC, Keck-II, and/or SPID facilities of Northwestern University's *NUANCE* Center, which is supported by the Soft and Hybrid Nanotechnology Experimental (SHyNE) Resource (NSF ECCS-1542205), the MRSEC program (NSF DMR-1121262) at the Materials Research Center, the International Institute for Nanotechnology (IIN), the Keck Foundation, and the State of Illinois, through the IIN. We thank Aifeng Wang at Brookhaven National Laboratory for useful discussions on the MR analysis.

References

1. Geim, A. K.; Grigorieva, I. V., Van der Waals heterostructures. *Nature* **2013**, *499* (7459), 419-425.
2. Nicolosi, V.; Chhowalla, M.; Kanatzidis, M. G.; Strano, M. S.; Coleman, J. N., Liquid exfoliation of layered materials. *Science* **2013**, *340* (6139), 1226-1229.
3. Novoselov, K. S.; Geim, A. K.; Morozov, S. V.; Jiang, D.; Zhang, Y.; Dubonos, S. V.; Grigorieva, I. V.; Firsov, A. A., Electric field effect in atomically thin carbon films. *Science* **2004**, *306* (5696), 666-669.
4. Radisavljevic, B.; Kis, A., Mobility engineering and a metal-insulator transition in monolayer MoS₂. *Nature Materials* **2013**, *12* (9), 815-820.
5. Lopez-Sanchez, O.; Lembke, D.; Kayci, M.; Radenovic, A.; Kis, A., Ultrasensitive photodetectors based on monolayer MoS₂. *Nature Nanotechnology* **2013**, *8* (7), 497-501.
6. Ali, M. N.; Xiong, J.; Flynn, S.; Tao, J.; Gibson, Q. D.; Schoop, L. M.; Liang, T.; Haldolaarachchige, N.; Hirschberger, M.; Ong, N., Large, non-saturating magnetoresistance in WTe₂. *Nature* **2014**, *514* (7521), 205-208.
7. Zhao, L.-D.; Lo, S.-H.; Zhang, Y.; Sun, H.; Tan, G.; Uher, C.; Wolverton, C.; Dravid, V. P.; Kanatzidis, M. G., Ultralow thermal conductivity and high thermoelectric figure of merit in SnSe crystals. *Nature* **2014**, *508* (7496), 373-377.
8. Zhao, L.-D.; Tan, G.; Hao, S.; He, J.; Pei, Y.; Chi, H.; Wang, H.; Gong, S.; Xu, H.; Dravid, V. P., Ultrahigh power factor and thermoelectric performance in hole-doped single-crystal SnSe. *Science* **2016**, *351* (6269), 141-144.
9. Park, J.; Lee, G.; Wolff-Fabris, F.; Koh, Y.; Eom, M.; Kim, Y.; Farhan, M.; Jo, Y.; Kim, C.; Shim, J., Anisotropic Dirac fermions in a Bi square net of SrMnBi₂. *Physical Review Letters* **2011**, *107* (12), 126402.
10. Liu, J.; Hu, J.; Zhang, Q.; Graf, D.; Cao, H. B.; Radmanesh, S.; Adams, D.; Zhu, Y.; Cheng, G.; Liu, X., A magnetic topological semimetal Sr_{1-y}Mn_{1-z}Sb₂ (y, z < 0.1). *Nature Materials* **2017**, *16* (9), 905-910.
11. Gong, C.; Li, L.; Li, Z.; Ji, H.; Stern, A.; Xia, Y.; Cao, T.; Bao, W.; Wang, C.; Wang, Y., Discovery of intrinsic ferromagnetism in two-dimensional van der Waals crystals. *Nature* **2017**, *546* (7657), 265.
12. Huang, B.; Clark, G.; Navarro-Moratalla, E.; Klein, D. R.; Cheng, R.; Seyler, K. L.; Zhong, D.; Schmidgall, E.; McGuire, M. A.; Cobden, D. H., Layer-dependent ferromagnetism in a van der Waals crystal down to the monolayer limit. *Nature* **2017**, *546* (7657), 270.
13. Song, T.; Cai, X.; Tu, M. W.-Y.; Zhang, X.; Huang, B.; Wilson, N. P.; Seyler, K. L.; Zhu, L.; Taniguchi, T.; Watanabe, K., Giant tunneling magnetoresistance in spin-filter van der Waals heterostructures. *Science* **2018**, eaar4851.
14. Jiang, S.; Shan, J.; Mak, K. F., Electric-field switching of two-dimensional van der Waals magnets. *Nature Materials* **2018**, *17*, 406-410.
15. Miao, N.; Xu, B.; Zhu, L.; Zhou, J.; Sun, Z., 2D Intrinsic Ferromagnets from van der Waals Antiferromagnets. *Journal of the American Chemical Society* **2018**, *140* (7), 2417-2420.
16. Mounet, N.; Gibertini, M.; Schwaller, P.; Campi, D.; Merkys, A.; Marrazzo, A.; Sohler, T.; Castelli, I. E.; Cepellotti, A.; Pizzi, G., Two-dimensional materials from high-

- throughput computational exfoliation of experimentally known compounds. *Nature Nanotechnology* **2018**, *13* (3), 246-252.
17. Seyler, K. L.; Zhong, D.; Klein, D. R.; Gao, S.; Zhang, X.; Huang, B.; Navarro-Moratalla, E.; Yang, L.; Cobden, D. H.; McGuire, M. A., Ligand-field helical luminescence in a 2D ferromagnetic insulator. *Nature Physics* **2018**, *14* (3), 277.
 18. Burch, K. S.; Mandrus, D.; Park, J.-G., Magnetism in two-dimensional van der Waals materials. *Nature* **2018**, *563* (7729), 47-52.
 19. Schoop, L. M.; Ali, M. N.; Straßer, C.; Topp, A.; Varykhalov, A.; Marchenko, D.; Duppl, V.; Parkin, S. S.; Lotsch, B. V.; Ast, C. R., Dirac cone protected by non-symmorphic symmetry and three-dimensional Dirac line node in ZrSiS. *Nature Communications* **2016**, *7*, 11696.
 20. Neupane, M.; Belopolski, I.; Hosen, M. M.; Sanchez, D. S.; Sankar, R.; Szlawska, M.; Xu, S.-Y.; Dimitri, K.; Dhakal, N.; Maldonado, P., Observation of topological nodal fermion semimetal phase in ZrSiS. *Physical Review B* **2016**, *93* (20), 201104.
 21. Singha, R.; Pariari, A. K.; Satpati, B.; Mandal, P., Large nonsaturating magnetoresistance and signature of nondegenerate Dirac nodes in ZrSiS. *Proceedings of the National Academy of Sciences* **2017**, 201618004.
 22. Effenberger, H.; Culetto, F.; Topa, D.; Paar, W., The crystal structure of synthetic buckhornite, [Pb₂BiS₃][AuTe₂]. *Zeitschrift für Kristallographie-Crystalline Materials* **2000**, *215* (1), 10-16.
 23. Fang, L.; Im, J.; Stoumpos, C. C.; Shi, F.; Dravid, V.; Leroux, M.; Freeman, A. J.; Kwok, W.-K.; Chung, D. Y.; Kanatzidis, M., Two-dimensional mineral [Pb₂BiS₃][AuTe₂]: High-mobility charge carriers in single-atom-thick layers. *Journal of the American Chemical Society* **2015**, *137* (6), 2311-2317.
 24. Fang, L.; Im, J.; DeGottardi, W.; Jia, Y.; Glatz, A.; Matveev, K.; Kwok, W.-K.; Crabtree, G.; Kanatzidis, M., Large spin-orbit coupling and helical spin textures in 2D heterostructure [Pb₂BiS₃][AuTe₂]. *Scientific Reports* **2016**, *6*, 35313.
 25. Kaden, R.; Wagner, G.; Sturm, C.; Schmidt-Grund, R.; von Wenckstern, H.; Prager, A.; Bente, K.; Grundmann, M., Synthesis and physical properties of cylindrite micro tubes and lamellae. *Physica Status Solidi (b)* **2010**, *247* (6), 1335-1350.
 26. Yudovskaya, M.; Trubkin, N.; Koporulina, E.; Belakovsky, D.; Mokhov, A.; Kuznetsova, M.; Golovanova, T., Abramovite, Pb₂SnInBiS₇, a new mineral species from fumaroles of the Kudryavy volcano, Kurile Islands, Russia. *Geology of Ore Deposits* **2008**, *50* (7), 551-555.
 27. Jaszczak, J. A.; Rumsey, M. S.; Bindi, L.; Hackney, S. A.; Wise, M. A.; Stanley, C. J.; Spratt, J., Merelaniite, Mo₄Pb₄VSbS₁₅, a new molybdenum-essential member of the cylindrite group, from the Merelani tanzanite deposit, Lelatema Mountains, Manyara Region, Tanzania. *Minerals* **2016**, *6* (4), 115.
 28. Moëlo, Y.; Makovicky, E.; Karup-Moller, S.; Cerville, B.; Maurel, C., La lévyclaudite, Pb₈Sn₇Cu₃(Bi,Sb)₃S₂₈, une nouvelle espèce à structure incommensurable, de la série de la cylindrite. *European Journal of Mineralogy* **1990**, 711-724.
 29. Bindi, L.; Paar, W. H., Jaszczakite, [(Bi,Pb)₃S₃][AuS₂], a new mineral species from Nagybörzsöny, Hungary. *European Journal of Mineralogy* **2017**, *29* (4), 673-677.
 30. Molina-Mendoza, A. J.; Giovanelli, E.; Paz, W. S.; Niño, M. A.; Island, J. O.; Evangeli, C.; Aballe, L.; Foerster, M.; Van Der Zant, H. S.; Rubio-Bollinger, G.,

Franckeite as a naturally occurring van der Waals heterostructure. *Nature Communications* **2017**, *8*, 14409.

31. Evain, M.; Petricek, V.; Moëlo, Y.; Maurel, C., First (3+ 2)-dimensional superspace approach to the structure of levyclaudite-(Sb), a member of the cylindrite-type minerals. *Acta Crystallographica Section B: Structural Science* **2006**, *62* (5), 775-789.
32. Makovicky, E.; Petricek, V.; Dusek, M.; Topa, D., Crystal structure of a synthetic tin-selenium representative of the cylindrite structure type. *American Mineralogist* **2008**, *93* (11-12), 1787-1798.
33. Malliakas, C. D.; Kanatzidis, M. G., Nb–Nb interactions define the charge density wave structure of 2H-NbSe₂. *Journal of the American Chemical Society* **2013**, *135* (5), 1719-1722.
34. Chen, H.; Malliakas, C. D.; Narayan, A.; Fang, L.; Chung, D. Y.; Wagner, L. K.; Kwok, W.-K.; Kanatzidis, M. G., Charge Density Wave and Narrow Energy Gap at Room Temperature in 2D Pb_{3-x}Sb_{1+x}S₄Te_{2-δ} with Square Te Sheets. *Journal of the American Chemical Society* **2017**, *139* (32), 11271-11276.
35. Sung, Y.-H.; Ciobanu, C.; Pring, A.; Brügger, J.; Skinner, W.; Cook, N.; Nugus, M., Tellurides from Sunrise Dam gold deposit, Yilgarn Craton, Western Australia: a new occurrence of nagyágite. *Mineralogy and Petrology* **2007**, *91* (3-4), 249-270.
36. Effenberger, H.; Paar, W. H.; Topa, D.; Culetto, F. J.; Giester, G., Toward the crystal structure of nagyagite, [Pb(Pb,Sb)S₂][(Au,Te)]. *American Mineralogist* **1999**, *84* (4), 669-676.
37. X-RED; X.-A. X.-S., *STOE & Cie GmbH: Darmstadt, Germany* **2009**.
38. Palatinus, L.; Chapuis, G., SUPERFLIP—a computer program for the solution of crystal structures by charge flipping in arbitrary dimensions. *Journal of Applied Crystallography* **2007**, *40* (4), 786-790.
39. Petříček, V.; Dušek, M.; Palatinus, L., Crystallographic computing system JANA2006: general features. *Zeitschrift für Kristallographie-Crystalline Materials* **2014**, *229* (5), 345-352.
40. Moritomo, Y.; Asamitsu, A.; Kuwahara, H.; Tokura, Y., Giant magnetoresistance of manganese oxides with a layered perovskite structure. *Nature* **1996**, *380* (6570), 141–144.
41. Baibich, M. N.; Broto, J. M.; Fert, A.; Van Dau, F. N.; Petroff, F.; Etienne, P.; Creuzet, G.; Friederich, A.; Chazelas, J., Giant magnetoresistance of (001)Fe/(001)Cr magnetic superlattices. *Physical Review Letters* **1988**, *61* (21), 2472.
42. Rettie, A. J. E.; Sturza, M.; Malliakas, C. D.; Botana, A. S.; Chung, D. Y.; Kanatzidis, M. G., Copper vacancies and heavy holes in the two-dimensional semiconductor KCu_{3-x}Se₂. *Chemistry of Materials* **2017**, *29* (14), 6114-6121.
43. Chen, H.; Rodrigues, J. N.; Rettie, A. J.; Song, T.-B.; Chica, D. G.; Su, X.; Bao, J.-K.; Chung, D. Y.; Kwok, W.-K.; Wagner, L. K., High Hole Mobility and Nonsaturating Giant Magnetoresistance in the New 2D Metal NaCu₄Se₄ Synthesized by a Unique Pathway. *Journal of the American Chemical Society* **2019**, *141* (1), 635–642.
44. Kresse, G.; Hafner, J., Ab initio molecular dynamics for open-shell transition metals. *Physical Review B* **1993**, *48* (17), 13115.
45. Kresse, G.; Furthmüller, J., Efficiency of ab-initio total energy calculations for metals and semiconductors using a plane-wave basis set. *Computational Materials Science* **1996**, *6* (1), 15-50.

46. Blöchl, P. E., Projector augmented-wave method. *Physical Review B* **1994**, 50 (24), 17953.
47. Kresse, G.; Joubert, D., From ultrasoft pseudopotentials to the projector augmented-wave method. *Physical Review B* **1999**, 59 (3), 1758.
48. Perdew, J. P.; Burke, K.; Ernzerhof, M., Generalized gradient approximation made simple. *Physical Review Letters* **1996**, 77 (18), 3865.
49. Geim, A. K., Graphene: status and prospects. *Science* **2009**, 324 (5934), 1530-1534.
50. Sze, S. M.; Ng, K. K., *Physics of semiconductor devices*. John Wiley & sons: 2006.
51. Mott, N., Conduction in glasses containing transition metal ions. *Journal of Non-Crystalline Solids* **1968**, 1 (1), 1-17.
52. Fang, L.; Iyer, R. G.; Tan, G.; West, D. J.; Zhang, S.; Kanatzidis, M. G., The New Phase [Tl₄Sb₆Se₁₀][Sn₅Sb₂Se₁₄]: A Naturally Formed Semiconducting Heterostructure with Two-Dimensional Conductance. *Journal of the American Chemical Society* **2014**, 136 (31), 11079-11084.
53. Yu, D.; Wang, C.; Wehrenberg, B. L.; Guyot-Sionnest, P., Variable range hopping conduction in semiconductor nanocrystal solids. *Physical review letters* **2004**, 92 (21), 216802.
54. Pedersen, K. S.; Perlepe, P.; Aubrey, M. L.; Woodruff, D. N.; Reyes-Lillo, S. E.; Reinholdt, A.; Voigt, L.; Li, Z.; Borup, K.; Rouzières, M., Formation of the layered conductive magnet CrCl₂(pyrazine)₂ through redox-active coordination chemistry. *Nature chemistry* **2018**, 10 (10), 1056-1061.
55. Peter, Y.; Cardona, M., *Fundamentals of semiconductors: physics and materials properties*. Springer Science & Business Media: 2010.
56. Lu, H.-Z.; Shen, S.-Q., Weak antilocalization and localization in disordered and interacting Weyl semimetals. *Physical Review B* **2015**, 92 (3), 035203.
57. Wang, Y.; Liu, E.; Liu, H.; Pan, Y.; Zhang, L.; Zeng, J.; Fu, Y.; Wang, M.; Xu, K.; Huang, Z., Gate-tunable negative longitudinal magnetoresistance in the predicted type-II Weyl semimetal WTe₂. *Nature Communications* **2016**, 7, 13142.
58. Li, Q.; Kharzeev, D. E.; Zhang, C.; Huang, Y.; Pletikosić, I.; Fedorov, A.; Zhong, R.; Schneeloch, J.; Gu, G.; Valla, T., Chiral magnetic effect in ZrTe₅. *Nature Physics* **2016**, 12 (6), 550-554.
59. Shi, Q.; Martin, P.; Ebner, Q.; Zudov, M.; Pfeiffer, L.; West, K., Colossal negative magnetoresistance in a two-dimensional electron gas. *Physical Review B* **2014**, 89 (20), 201301.
60. Breunig, O.; Wang, Z.; Taskin, A.; Lux, J.; Rosch, A.; Ando, Y., Gigantic negative magnetoresistance in the bulk of a disordered topological insulator. *Nature Communications* **2017**, 8, 15545.
61. Ramirez, A., Colossal magnetoresistance. *Journal of Physics: Condensed Matter* **1997**, 9 (39), 8171.
62. Ramirez, A.; Cava, R.; Krajewski, J., Colossal magnetoresistance in Cr-based chalcogenide spinels. *Nature* **1997**, 386 (6621), 156.
63. Son, D.; Spivak, B., Chiral anomaly and classical negative magnetoresistance of Weyl metals. *Physical Review B* **2013**, 88 (10), 104412.

64. Burkov, A., Chiral anomaly and diffusive magnetotransport in Weyl metals. *Physical Review Letters* **2014**, *113* (24), 247203.
65. Huang, X.; Zhao, L.; Long, Y.; Wang, P.; Chen, D.; Yang, Z.; Liang, H.; Xue, M.; Weng, H.; Fang, Z., Observation of the chiral-anomaly-induced negative magnetoresistance in 3D Weyl semimetal TaAs. *Physical Review X* **2015**, *5* (3), 031023.
66. Grüner, G., Density Waves in Solids. *Addison-Wesley: Reading, PA*, **1994**.

Table 1. Crystallographic data and structure refinement for Pb_{3.1}Sb_{0.9}S₄Au_{0.52}Te_{1.48} and Pb_{3.1}Sb_{0.9}S₄Au_{0.44}Te_{1.56} at 293 K

Empirical formula	Pb _{3.1} Sb _{0.9} S ₄ Au _{0.52} Te _{1.48}	Pb _{3.1} Sb _{0.9} S ₄ Au _{0.44} Te _{1.56}
Formula weight	1169.5	1165.8
Crystal system	Monoclinic	Monoclinic
Space group	<i>P</i> 2 ₁ / <i>m</i> (<i>a</i> 0 γ)00	<i>P</i> 2 ₁ / <i>m</i>
Unit cell dimensions	<i>a</i> = 4.1721(4) Å, α = 90° <i>b</i> = 4.1512(4) Å, β = 95.814(8)° <i>c</i> = 15.1271(15) Å, γ = 90°	<i>a</i> = 4.1775(5) Å, α = 90° <i>b</i> = 4.1687(3) Å, β = 95.710(9)° <i>c</i> = 15.1318(18) Å, γ = 90°
<i>q</i> -vector	1/3 <i>a</i> * – 1/3 <i>c</i> *	
Volume, <i>Z</i>	260.64(4) Å ³ , 1	262.21(5) Å ³ , 1
Density (calculated)	7.451 g/cm ³	7.383 g/cm ³
Crystal size	0.201 × 0.109 × 0.005 mm ³	0.854 × 0.717 × 0.074 mm ³
θ range for data collection	2.71 to 29.32°	4.06 to 29.26°
Index ranges	-6 ≤ <i>h</i> ≤ 5, -5 ≤ <i>k</i> ≤ 5, -21 ≤ <i>l</i> ≤ 21, -1 ≤ <i>m</i> ≤ 1	-5 ≤ <i>h</i> ≤ 5, -5 ≤ <i>k</i> ≤ 5, -20 ≤ <i>l</i> ≤ 20
Reflections collected	14870 (4930 main + 9940 satellites)	4962
Independent reflections	2392 (795 main + 1597 satellites) [<i>R</i> _{int} = 0.0818]	795 [<i>R</i> _{int} = 0.0799]
Final <i>R</i> indices [<i>I</i> > 2σ(<i>I</i>)]	<i>R</i> _{obs} = 0.0520, <i>wR</i> _{obs} = 0.1086	<i>R</i> _{obs} = 0.0714, <i>wR</i> _{obs} = 0.1516
<i>R</i> indices [all data]	<i>R</i> _{all} = 0.1082, <i>wR</i> _{all} = 0.1116	<i>R</i> _{all} = 0.0823, <i>wR</i> _{all} = 0.1519
Final <i>R</i> main indices [<i>I</i> > 2σ(<i>I</i>)]	<i>R</i> _{obs} = 0.0451, <i>wR</i> _{obs} = 0.1079	
<i>R</i> main indices (all data)	<i>R</i> _{all} = 0.0494, <i>wR</i> _{all} = 0.1081	
Final <i>R</i> 1 st order satellites [<i>I</i> > 2σ(<i>I</i>)]	<i>R</i> _{obs} = 0.0913, <i>wR</i> _{obs} = 0.1164	
<i>R</i> 1 st order satellites (all data)	<i>R</i> _{all} = 0.2916, <i>wR</i> _{all} = 0.1441	

$R = \Sigma||F_o| - |F_c|| / \Sigma|F_o|$, $wR = \{\Sigma[w(|F_o|^2 - |F_c|^2)^2] / \Sigma[w(|F_o|^4)]\}^{1/2}$ and $w = 1/(\sigma^2(I) + 0.0004I^2)$. Wavelength (0.71073 Å).

Table 2. Comparison of the composition, Au:Te molar ratio, Au³⁺, Te⁻ and Te²⁻ amounts, resistivity (ρ), carrier density (n), and carrier mobility (μ) at 300 and 2 K for the mineral nagyágite [Pb_{3.1}Sb_{0.9}S₄][Au_{*x*}Te_{2-*x*}].

x	Au:Te ratio	Au ³⁺	Te ⁻	Te ²⁻	Structure modulation	ρ , 300 K (Ω cm)	ρ , 2 K (Ω cm)	n , 300 K (10 ¹⁸ cm ⁻³)	n , 2 K (10 ¹⁷ cm ⁻³)	μ , 300 K (cm ² V ⁻¹ s ⁻¹)	μ , 2 K (cm ² V ⁻¹ s ⁻¹)
0.52	1:2.8	0.52	0.5	0.98	Yes	0.00577	0.054	4.14	8.14	261.2	142.7
0.5	1:3	0.5	0.6	0.9	No	0.00683	0.115	3.06	3.27	299.1	165.7
0.44	1:3.5	0.44	0.9	0.66	No	0.00833	7.225	1.61	0.21	466.3	41.1
0.4	1:4	0.4	1.1	0.5	No	0.01	39.183	0.8	5.03×10 ⁻²	773.9	31.7
0.36	1:4.5	0.36	1.3	0.34	No	0.0126	8.26×10 ⁴	0.367	4.16×10 ⁻⁴	1351.8	1.82

Figure Captions

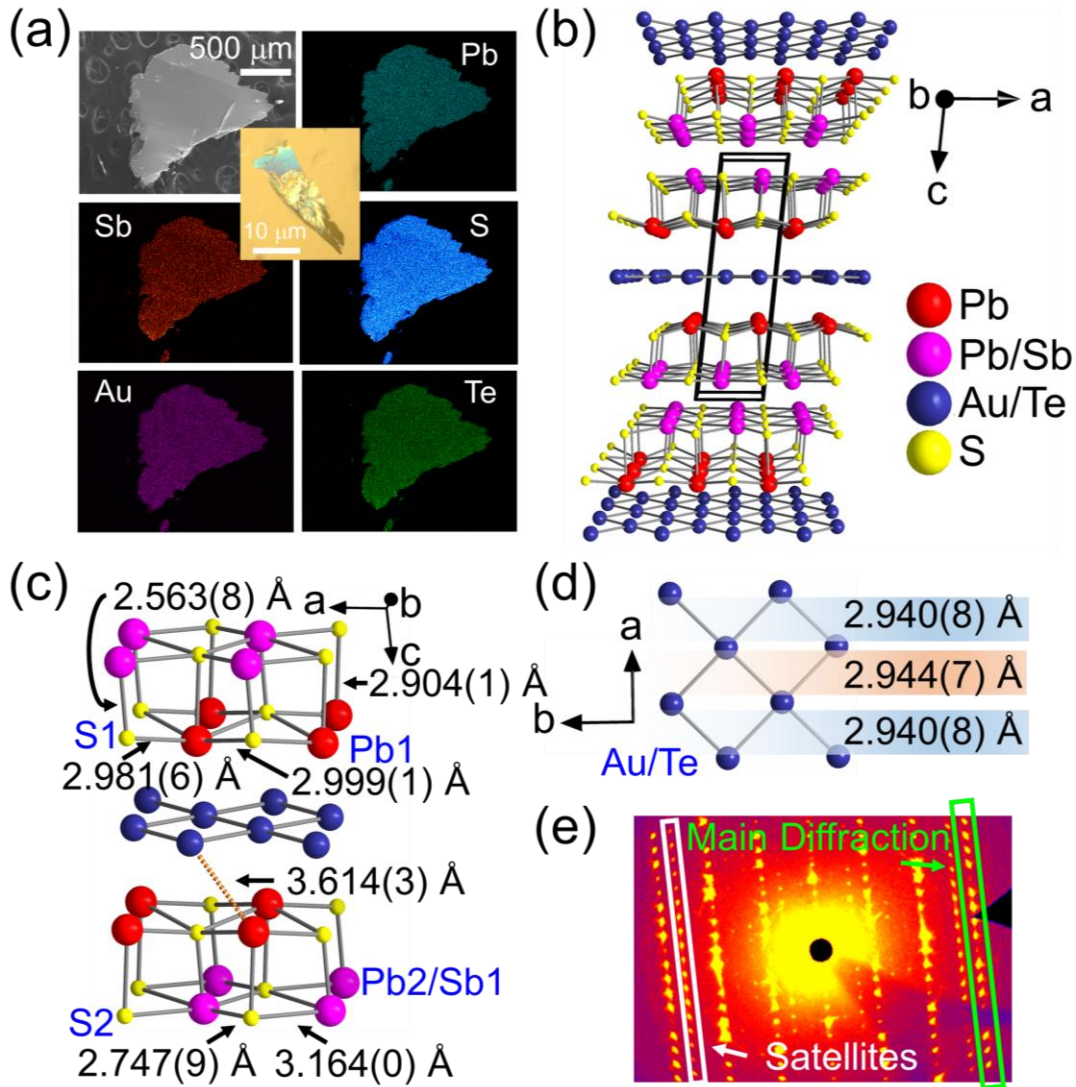


Figure 1. (a) SEM image of a single crystal with a smooth surface and EDS mapping of the as-grown plate. The inset is an optical image of a cleaved crystal that shows sea-green pigment in the thinner layer and golden or black color in the thicker part. (b) Average structure of the mineral $[\text{Pb}_{3.1}\text{Sb}_{0.9}\text{S}_4][\text{Au}_{0.52}\text{Te}_{1.48}]$ with alternating $[\text{Pb}_{3.1}\text{Sb}_{0.9}\text{S}_4]$ slabs and square $[\text{Au}_{0.52}\text{Te}_{1.48}]$ sheets. (c) Side-view of the average structure. Bonds between the two different layers indicate a weak interlayer interaction. (d) Au/Te distances in the square sheets in the average structure. (e) A processed reciprocal lattice image from the X-ray diffraction data along the $[0\ 1\ 0]$ zone at room temperature. There are obvious satellite reflections around the main Bragg diffractions peaks, indicating a commensurately modulated superlattice ($3\times 1\times 3$).

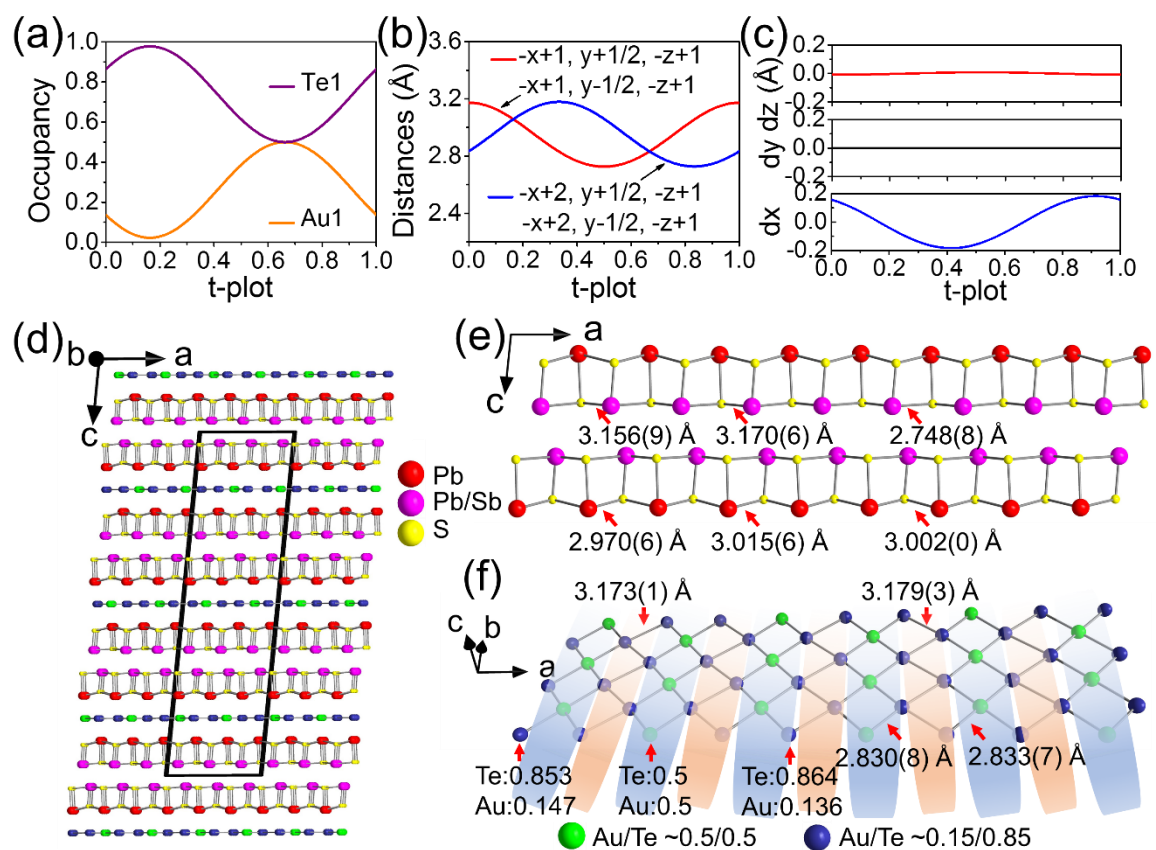


Figure 2. (a) Au/Te occupancy, (b) Au/Te-Au/Te distances (Å), (c) displacement parameters (Å) along the a , b , and c axes of Au/Te atoms in the modulated crystallographic model as a function of t -coordinate for $[\text{Pb}_{3.1}\text{Sb}_{0.9}\text{S}_4][\text{Au}_{0.52}\text{Te}_{1.48}]$. (d) The actual $3 \times 1 \times 3$ superlattice. Evolution of the modulated structure and bond distances in the (e) $[\text{Pb}_{3.1}\text{Sb}_{0.9}\text{S}_4]$ slabs and (f) $[\text{Au}_{0.52}\text{Te}_{1.48}]$ sheets.

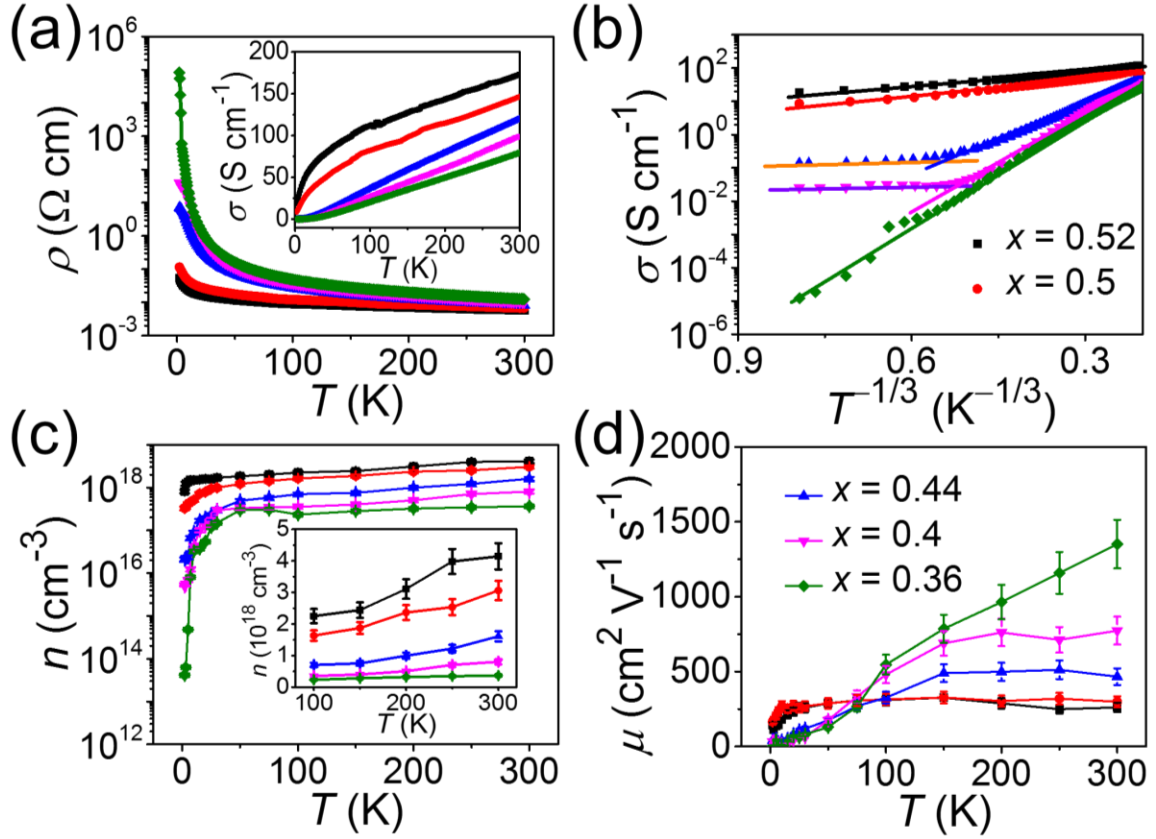


Figure 3. (a) Temperature dependence of the in-plane resistivity (ρ) of $[\text{Pb}_{3.1}\text{Sb}_{0.9}\text{S}_4][\text{Au}_x\text{Te}_{2-x}]$ ($x = 0.52 - 0.36$) single crystals from 300 to 2 K. Inset shows the corresponding temperature dependence of the conductivity (σ). (b) All the curves of σ below 100 K are well fitted using the model of 2D electron variable range hopping. For the $x = 0.44$ and 0.4 samples, the conductivity displays crossovers at ~ 8 K, which is because of different hopping distances. (c) Carrier concentration (n) (inset: n between 100 and 300 K) and (d) carrier mobility (μ) as a function of temperature.

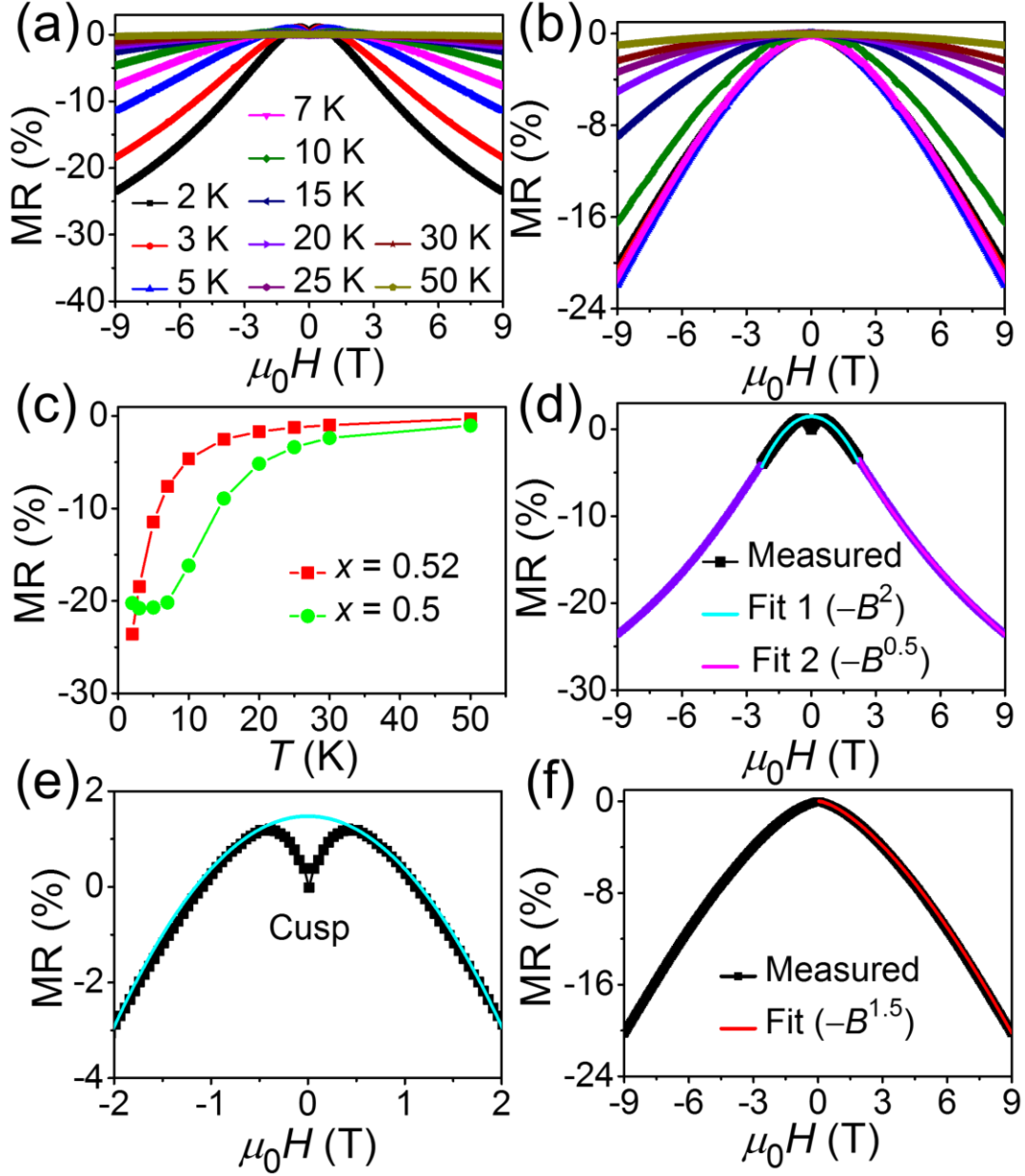


Figure 4. Magnetic field dependence of the magnetoresistance (MR), defined as $[\rho(H) - \rho(0)]/\rho(0) \times 100\%$, at different temperatures for (a) $[\text{Pb}_{3.1}\text{Sb}_{0.9}\text{S}_4][\text{Au}_{0.52}\text{Te}_{1.48}]$ and (b) $[\text{Pb}_{3.1}\text{Sb}_{0.9}\text{S}_4][\text{Au}_{0.5}\text{Te}_{1.5}]$. Temperature dependence of the MR at ± 9 T for (c) $[\text{Pb}_{3.1}\text{Sb}_{0.9}\text{S}_4][\text{Au}_{0.52}\text{Te}_{1.48}]$ and $[\text{Pb}_{3.1}\text{Sb}_{0.9}\text{S}_4][\text{Au}_{0.5}\text{Te}_{1.5}]$. (d) The MR for $[\text{Pb}_{3.1}\text{Sb}_{0.9}\text{S}_4][\text{Au}_{0.52}\text{Te}_{1.48}]$ at 2 K implies two regions. The one under $0 \text{ T} < B < 2.2 \text{ T}$ is with respect to $-B^2$ (fit 1), the other under $2.2 \text{ T} < B < 9 \text{ T}$ is to $-B^{0.5}$ (fit 2). (e) MR show a small cusp under $-0.5 \text{ T} < B < 0.5 \text{ T}$. (f) The MR for $[\text{Pb}_{3.1}\text{Sb}_{0.9}\text{S}_4][\text{Au}_{0.5}\text{Te}_{1.5}]$ at 2 K can be fitted entirely based on $-B^{1.5}$ dependence.

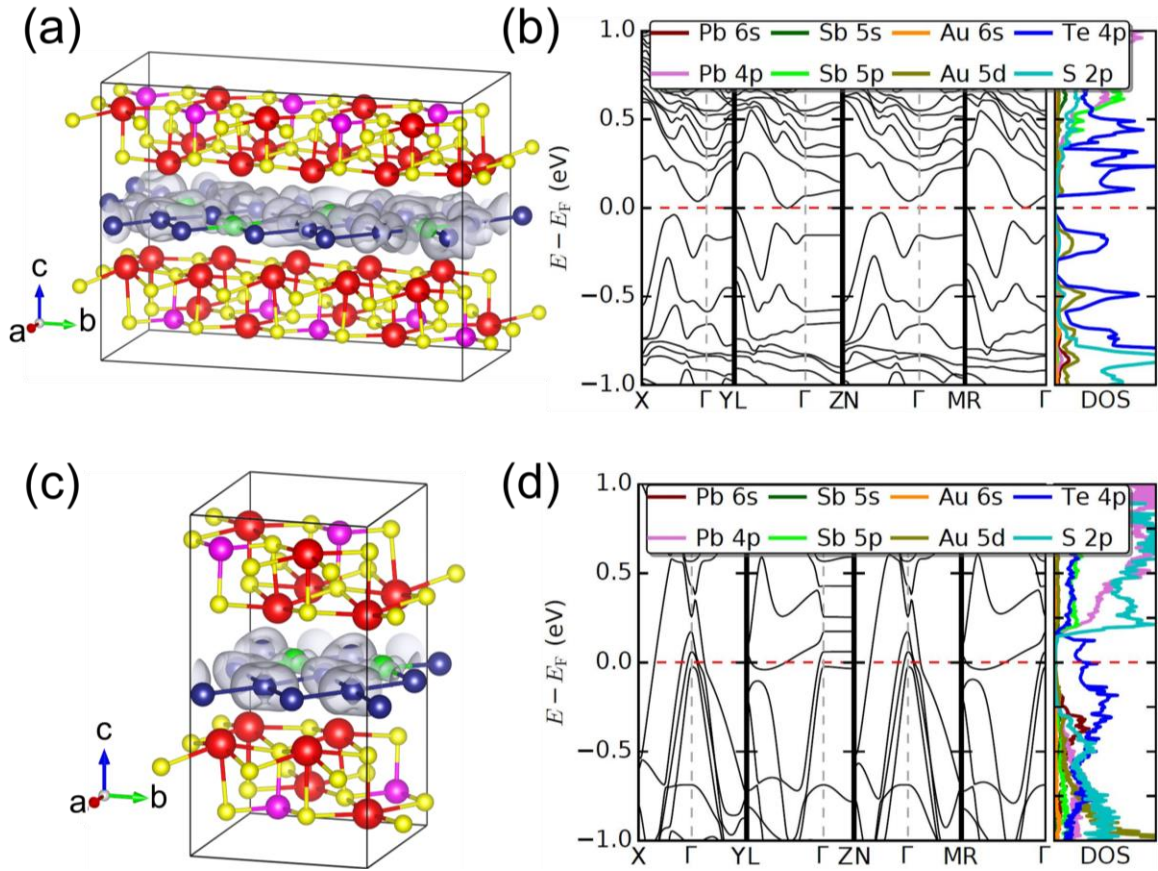


Figure 5. (a) The isosurface of electron density around the Fermi level, (b) band structure and density of states of $\text{Pb}_{30}\text{Sb}_{10}\text{S}_{40}\text{Au}_4\text{Te}_{16}$ in a $2 \times 5 \times 1$ supercell with $\text{Au}:\text{Te} = 1:4$. (c) The isosurface of electron density around the Fermi level, (d) band structure and density of states of $\text{Pb}_{12}\text{Sb}_4\text{S}_{16}\text{Au}_2\text{Te}_6$ in a $2 \times 2 \times 1$ supercell with $\text{Au}:\text{Te} = 1:3$.

For Table of Contents Only

